Density Functional Study of Ground and Excited States of $Mn_2(CO)_{10}$

Angela Rosa,[†] Giampaolo Ricciardi,[†] Evert Jan Baerends,*[,‡] and Derk J. Stufkens[§]

Dipartimento di Chimica, Universitá della Basilicata, Via N. Sauro, 85, 85100 Potenza, Italy, Afdeling Theoretische Chemie, Vrije Universiteit, De Boelelaan 1083, 1081 HV Amsterdam, The Netherlands, and Anorganisch Chemisch Laboratorium, Nieuwe Achtergracht 166, Universiteit van Amsterdam, 1018 WV Amsterdam, The Netherlands

Received July 19, 1994[⊗]

The precise nature of the excited states of $Mn_2(CO)_{10}$ leading to the well-known photochemistry—both Mn−Mn and Mn−CO bond breaking upon low-energy excitation—is still unclear. In order to identify possibly dissociative excited states (either Mn−Mn, Mn−CO_{ax}, or Mn−CO_{eq}), the nature of the highest occupied Mn-3d orbitals is analyzed as well as the composition of the virtual orbitals. The following features are noted. (a) The low-energy excitations at 337−355 nm arise from $\sigma \rightarrow \sigma^*$ and $d\pi \rightarrow \sigma^*$ excitations, while d → d excitations occur at much higher energy. (b) The Mn−Mn σ bonding HOMO as well as the σ^* LUMO cannot simply be classified as arising from the $3d_{z^2}$ components of e_g parentage in the local octahedrons around Mn, they have little $3d_{z^2} - 3d_{z^2}$ (anti)bonding character but significant contributions come from Mn−$4p_z$ and CO-$2\pi_{eq}$ orbitals. Mn−Mn σ antibonding is only strong in the σ^* orbital due to these contributions. (c) Due to the strong involvement of Mn−$4p_z$, th $3d_{z^2}$ orbital not only occurs in the σ and σ^* orbitals but also in a higher set of virtuals, denoted σ',σ'^*, ~1.5 eV above the σ^* orbital. Antibonding with axial CO's is strong in these higher virtuals but absent or weak in the σ and σ^* orbitals. σ antibonding with equatorial CO's is strong in the $3d_{x^2-y^2}$ orbital of e_g parentage, that is located very high in the virtual spectrum, ~2 eV above the σ^* orbital. Mn−Mn dissociation will occur only from the $\sigma \rightarrow \sigma^*$ excitation; CO loss will probably occur from the high-lying d → d excited states (excitations into σ',σ'^* and $3d_{x^2-y^2}$). The observed photochemistry at low energy will have to be explained from curve crossings between the low-energy excited states and the photoactive states.

Introduction

$Mn_2(CO)_{10}$ has attracted considerable interest mostly because of its rich photochemistry that is generally taken as a prototype for photoreactions of organometallic compounds containing metal−metal bonds.[1−4] Two primary photochemical reaction pathways have been established[5−13] in the condensed-phase photolysis of $Mn_2(CO)_{10}$: metal−metal bond cleavage to produce $Mn(CO)_5$ radicals (eq 1) and dissociative loss of CO to give $Mn_2(CO)_9$ without metal−metal bond cleavage (eq 2).

$$Mn_2(CO)_{10} \xrightarrow{h\nu} 2Mn(CO)_5 \quad (1)$$

$$Mn_2(CO)_{10} \xrightarrow{h\nu} Mn_2(CO)_9 + CO \quad (2)$$

The relative quantum yield for these two channels depends on the excitation wavelength. Generally it was found that low energy excitation favors metal−metal bond homolysis, while higher energy excitation leads mostly to the generation of $Mn_2(CO)_9$. Kobayashi *et al.*[14] have measured the quantum yields of processes (1) and (2), Y_1 and Y_2, at different excitation wavelengths. They obtained ratio $R = Y_1/Y_2$ of 0.19, 0.43, and 1.1 at λ_{ex} = 266, 337, and 355 nm respectively. Gas-phase photodissociation studies[15] of $Mn_2(CO)_{10}$ are largely consistent with the photochemistry of the molecule in solution. In spite of the intense experimental work on the photochemistry of $Mn_2(CO)_{10}$ during the last decade, mainly due to the availability of more and more sophisticated identification techniques, the mechanism of the primary photochemical processes is far from being understood. Full elucidation of these processes would require a study based on the calculations of the potential energy surfaces (PES) or the more readily visualized potential energy curves (PEC), giving the energy *versus* one geometrical coordinate, which connect the ground and excited states of the reactant with the ground and excited states of the primary products. These curves provide the most important features of the energy profile of the primary photodissociative pathways, as proved for a number of organometallic systems.[16−23]

[†] Universitá della Basilicata.
[‡] Vrije Universiteit.
[§] Universiteit van Amsterdam.
[⊗] Abstract published in *Advance ACS Abstracts,* May 15, 1995.

(1) (a) Geoffroy, G. L.; Wrighton, M. S. *Organometallic Photochemistry*; Academic: New York, 1979. (b) Geoffroy, G. L. *J. Chem. Educ.* **1983**, *60*, 861.
(2) Wegman, R. W.; Olsen, R. J.; Gard, D. R.; Faulkner, L. R.; Brown, T. L. *J. Am. Chem. Soc.* **1981**, *103*, 6089.
(3) Wrighton, M. S.; Ginley, D. S. *J. Am. Chem. Soc.* **1975**, *97*, 2065.
(4) Stufkens, D. J. *Coord. Chem. Rev.* **1990**, *104*, 39.
(5) Yasufuku, K.; Kobayashi, T.; Iwai, J.; Yesaka, H.; Noda, H.; Ohtani, H. *Coord. Chem. Res.* **1985**, *64*, 1.
(6) Rothberg, L. J.; Cooper, N. J.; Peters, K. S.; Vaida, V. *J. Am. Chem. Soc.* **1984**, *104*, 3536.
(7) Church, S. P.; Herman, H.; Grevels, F.-W.; Schaffner, K. *J. Chem. Soc., Chem. Commun.* **1984**, 785 and references therein.
(8) Hepp, A. F.; Wrighton, M. S. *J. Am. Chem. Soc.* **1983**, *105*, 5934.
(9) Leopold, D. G.; Vaida, V. *J. Am. Chem. Soc.* **1984**, *106*, 3720.
(10) (a) Walker, H. W.; Herrick, R. S.; Olsen, R. J.; Brown, T. L. *Inorg. Chem.* **1984**, *23*, 3748. (b) Herrick, R. S.; Brown, T. L. *Inorg. Chem.* **1984**, *23*, 4550.
(11) Yesaka, H.; Kobayashi, T.; Yasufuku, K.; Nagakura, S. *J. Am. Chem. Soc.* **1983**, *105*, 6249.
(12) Zhang, J. Z.; Harris, C. B. *J. Chem. Phys.* **1991**, *95*, 4024.
(13) Joly, A. G.; Nelson, K. A. *Chem. Phys.* **1991**, *152*, 69.
(14) Kobayashi, T.; Ohtani, H.; Noda, H.; Teratani, S.; Yamazaki, H.; Yasufuku, K. *Organometallics* **1986**, *5*, 110.
(15) Prinslow, D. A.; Vaida, V. *J. Am. Chem. Soc.* **1987**, *109*, 5097.
(16) Daniel, C.; Bénard, M.; Dedieu, A.; Wiest, R.; Veillard, A. *J. Phys. Chem.* **1984**, *88*, 4805.
(17) Daniel, C.; Hyla-Kryspin, I.; Demuynck, J.; Veillard, A. *Nouv. J. Chim.* **1985**, *9*, 581.
(18) Veillard, A.; Daniel, C.; Strich, A. *Pure Appl. Chem.* **1988**, *60*(2), 215.
(19) Veillard, A.; Strich, A. *J. Am. Chem. Soc.* **1988**, *110*, 3793.
(20) Daniel, C. *Coordination Chemistry Reviews: Proceedings of the 8th International Symposium on the Photochemistry and Photophysics of Coordination Compounds*; 1990; Elsevier Science Publishers B.V.: Amsterdam, 1990; Vol. 97, p 141.
(21) Daniel, C. *J. Phys. Chem.* **1991**, *95*, 2394.
(22) Rohmer, M. M.; Veillard, A. *New J. Chem.* **1991**, *15*, 795.
(23) Daniel, C. *J. Am. Chem. Soc.*, **1992**, *114*, 1625.

0020-1669/95/1334-3425$09.00/0

Knowledge of the nature of the excited states which may play a role in the photodissociation processes constitutes, however, the first step of a more complete study based on the PEC. Meyer and Caspar[24] reviewed the interpretation of the photochemistry of $Mn_2(CO)_{10}$, making certain assumptions about the nature of the low energy excitations. To explain the occurrence of two primary photoprocesses, CO loss and Mn−Mn bond breaking, for $Mn_2(CO)_{10}$ at 337−355 nm these authors argue that CO loss most probably occurs from a d → d excited state, in analogy with monomeric complexes. It is therefore assumed that the shoulder (around 374 nm) to the red of the first intense UV absorption band around 336 nm, which is assigned[25] to a transition between the σ and σ^* orbitals associated with the metal−metal bond, arises from a $d\pi, d\delta(t_{2g}) \rightarrow d\delta(e_g)$ transition. Here $d\delta(e_g)$ (called $d\sigma^*$ by Meyer and Caspar) denotes the $d_{x^2-y^2}$ at the left Mn and the d_{xy} at the right Mn, which are antibonding with respect to the 5σ orbitals (C lone pairs) of the equatorial CO's. [Since we will stick to a notation where the σ, π, and δ labels refer to the Mn−Mn axis we call this orbital $d\delta$. The d_{xy} orbital at the left Mn and the $d_{x^2-y^2}$ at the right Mn, which also have δ symmetry with respect to the Mn−Mn bond axis, are denoted as $d\delta(t_{2g})$ since they are occupied t_{2g} orbitals in the local pseudooctahedral symmetry, strongly stabilized by π-back-bonding with equatorial carbonyls (see Figure 3 for choice of coordinate axes).] Electronic occupation of $d\delta(e_g)$ following $d(t_{2g}) \rightarrow d\delta(e_g)$ excitation is predicted to lead to labilization of equatorial COs. Therefore CO loss would occur from the $d \rightarrow d\delta(e_g)$ and Mn−Mn cleavage from the $^3(\sigma \rightarrow \sigma^*)$ photoactive excited states respectively. Intersection between the $^3(\sigma \rightarrow \sigma^*)$ and $(d \rightarrow d\delta(e_g))$ potential energy surfaces might then provide the clue for explaining the wavelength independence of the photochemistry of $Mn_2(CO)_{10}$ in the range 337−355 nm. In fact, if intersection between the two states occurs below the energies of the two transitions, the intersection can be reached from either transition and photolysis into either transition could give the same photoproducts.

The assumption that the $d\delta(e_g)$ would lie below or at least close to the σ^*, so that Mn−CO bond breaking ligand field (LF) type excitations are close in energy to the $\sigma \rightarrow \sigma^*$ excitation, is however not in agreement with the calculations of Levenson and Gray.[25] The lowest energy visible absorption around 374 nm has been assigned by these authors to a $d\pi^* \rightarrow \sigma^*$ transition. Caspar and Meyer argue that in that case the resulting excited state has to be responsible for *both* types of photochemistry. They consider this less likely, although not totally unreasonable since excitation of one electron from the $d\pi^*$ into the σ^* orbital would populate the σ^* Mn−Mn antibonding orbital, leading to labilization of the Mn−Mn bond, and would depopulate the $d\pi-2\pi$ Mn−CO bonding orbital (a "t_{2g}" orbital in the local pseudooctahedral symmetry) leading to CO labilization. UV excitation into the $^{1,3}(\sigma\sigma^*)$ state will lead to Mn−Mn bond cleavage directly but will lead to the same photoproducts as in the case of $d\pi^* \rightarrow \sigma^*$ excitation if the transition $^{1,3}(\sigma\sigma^*) \rightarrow (d\pi^*\sigma^*)$ occurs with high efficiency.

Apart from the questions raised above, one may also wonder whether the $\sigma \rightarrow \sigma^*$ excited state is maybe dissociative for both Mn−Mn bond breaking and CO loss, a phenomenon studied by Daniel, Veillard et al.[17,19] for $HCo(CO)_4$, and whether equatorial or axial CO loss occurs. The arguments by Meyer and Caspar[24] are conceptually appealing. In order to establish which one of the possibilities they advance is actually realized, accurate calculations of the excitation energies and of the electronic structure of the ground state and excited states are required.

The aim of this study is to locate the possible photoactive excited states of $Mn_2(CO)_{10}$. To this purpose the nature of the excited states involved in the electronic spectrum of this compound and their corresponding excitation energies are investigated by density functional calculations. A subsequent study concerning the ground- and excited-state potential energy curves corresponding to the homolysis of the Mn−Mn bond and to the dissociation of either an equatorial or an axial carbonyl ligand will be reported elsewhere.[26]

Method and Computational Details

The calculations reported in this paper are based on the Amsterdam Density Functional program package ADF,[27,28] characterized by the use of a density fitting procedure to obtain accurate Coulomb and exchange potentials in each SCF cycle, by accurate and efficient numerical integration of the effective one-electron hamiltonian matrix elements and by the possibility to freeze core orbitals. The molecular orbitals were expanded in an uncontracted double-ζ STO basis set for all atoms with the exception of the 3d Mn orbitals for which we used a triple-ζ STO basis set, and the Mn 4p for which one 4p STO was used. The cores (Mn, 1s−2p; C, O, 1s) have been kept frozen.

The LSD exchange potential was used,[29] together with the Vosko−Wilk−Nusair[30] parametrization of electron gas data for the local density approximation of the correlation energy. The ground and excited state energies included Becke's[31] nonlocal corrections to the local expression of the exchange energy and Perdew's[32] nonlocal corrections to the local expression for the correlation energy. The excitation energies have been calculated with a method, originally introduced by Ziegler *et al.*, that until now has been generally used for excitation energies in DFT.[33] In this method the final state relaxation effects are incorporated since separate SCF calculations are performed on the determinantal states representing pure-state densities for selected states out of a multiplet. This method has been discussed for atomic multiplet splittings by Von Barth[33b] and Lannoo, Baraff, and Schlüter[33c] (see also Wood[33d]). A recent application in transition metal chemistry and further references may be found in ref 33e. For those excited states that are the lowest state of their symmetry this method has the same justification as exists for the usual DFT ground state calculations. For higher excited states a formal justification is less straightforward. Therefore, even if the method has a good record of successful comparison to experiment, we will avoid putting too much emphasis on the quantitative values of the higher excitation energies, but we will be primarily concerned with the qualitative nature of the high lying states.

$Mn_2(CO)_{10}$ and $Mn(CO)_5$ geometries were optimized at the LSD level of theory using gradient techniques.[34]

As for the $Mn(CO)_5$ radical, experiments by Church *et al.*[35] have demonstrated that this species has square-pyramidal C_{4v} structure with

(24) Mayer, T. J.; Caspar, J. V. *Chem. Rev.* **1985**, *85*, 187.
(25) (a) Levenson, R. A.; Gray, H. B.; Ceasar, G. P. *J. Am. Chem. Soc.* **1970**, *92*, 3653. (b) Levenson, R. A.; Gray, H. B. *J. Am. Chem. Soc.* **1975**, *97*, 6042.
(26) Rosa, A.; Ricciardi, G.; Baerends, E. J.; Stufkens, D. J. Manuscript in preparation.
(27) (a) Baerends, E. J.; Ellis, D. E.; Ros, P. *Chem. Phys.* **1973**, *2*, 42. (b) Baerends, E. J.; Ros, P. *Int. J. Quantum Chem.* **1978**, *S12*, 169. (c) Boerrigter, P. M.; te Velde, G.; Baerends, E. J. *Int. J. Quantum Chem.* **1988**, *33*, 87.
(28) (a) Boerrigter, P. M.; te Velde, G.; Baerends, E. J. *Int. J. Quantum Chem.* **1988**, *33*, 87. (b) Te Velde, G.; Baerends, E. J. *J. Comput. Phys.*, **1992**, *99*, 84.
(29) Parr, R. G.; Yang, W. *Density-Functional Theory of Atoms and Molecules*; Oxford University Press: New York, 1989.
(30) Vosko, S. H.; Wilk, L.; Nusair, M. *J. Can. J. Phys.* **1980**, *58*, 1200.
(31) (a) Becke, A. D. *J. Chem. Phys.* **1986**, *84*, 4524. (b) Becke, A. D. *Phys. Rev.* **1988**, *A38*, 3098.
(32) (a) Perdew, J. P. *Phys. Rev.* **1986**, *B33*, 8822. (b) Perdew, J. P. *Phys. Rev.* **1986**, *B34*, 7406.
(33) (a) Ziegler, T.; Rauk, A.; Baerends, E. J. *Theor. Chim. Acta* **1977**, *43*, 261; (b) von Barth, U. *Phys. Rev.* **1979**, *A20*, 1693; (c) Lannoo, M.; Baraff, G. A.; Schlüter, M. *Phys. Rev.* **1981**, *B24*, 943; (d) Wood, J. H. *J. Phys. B: At. Mol. Phys.* **1980**, *13*, 1; (e) Daul, C.; Baerends, E. J.; Vernooijs, P. *Inorg. Chem.* **1994**, *33*, 3543.
(34) Versluis, L.; Ziegler, T. *J. Chem. Phys.* **1988**, *88*, 322.
(35) Church, S. P.; Poliakoff, M.; Timney, J. A.; Turner, J. J. *J. Am. Chem. Soc.* **1981**, *103*, 7515.

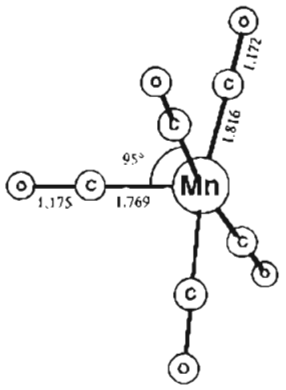

Figure 1. Optimized structure of $Mn(CO)_5$ in C_{4v} symmetry (bond distances in Å).

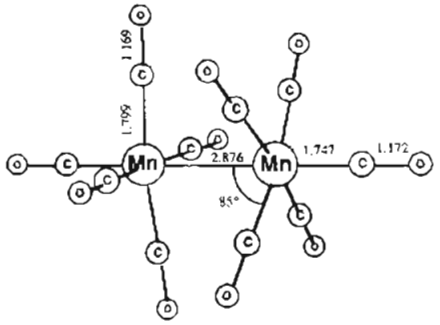

Figure 2. Optimized structure of $Mn_2(CO)_{10}$ in D_{4d} symmetry (bond distances in Å).

an apical-basal Mn−CO bond angle of 96 ± 3°. Recent calculations[23,36] also give the C_{4v} structure as the most stable one. Thus only this structure has been considered. The calculated bond parameters shown in Figure 1 confirm that the four equatorial CO ligands are bent slightly away (95°) from the apical ligand. As for $Mn_2(CO)_{10}$, electron diffraction in the gas phase,[37] X-ray diffraction at room temperature[38] and at 74 K[39] indicate a near-D_{4d} symmetry. Density functional calculations by Folga and Ziegler[40] give the eclipsed structure (D_{4h}) as higher in energy by 142.4 kJmol^{-1} than the staggered one. The structural parameters that we found for the D_{4d} staggered conformation of $Mn_2(CO)_{10}$ are shown in Figure 2. They do not differ significantly from those calculated by Folga and Ziegler[40] making full use of the self-consistent implementation[41-44] of nonlocal corrections (Becke−Perdew) in the geometry optimization.[41] There is a good agreement between theoretical and experimental geometry. In particular, the theoretical Mn−Mn bond distance of 2.865 Å is only 0.02 Å shorter than the most recent experimental value obtained by X-ray diffraction at 74 K[39] and is comparable to the value of 2.876 Å resulting from recent CI calculations.[45] Other experimental determinations of the Mn−Mn bond length by diffraction in the gas phase[38] and by X-ray diffraction at room temperature[39] resulted in longer bonds, i.e. 2.977 and 2.923 Å, respectively.

Ground State Electronic Structure

The electronic structure of $Mn_2(CO)_{10}$ has already been investigated by a number of theoretical approaches.[25,46-50]

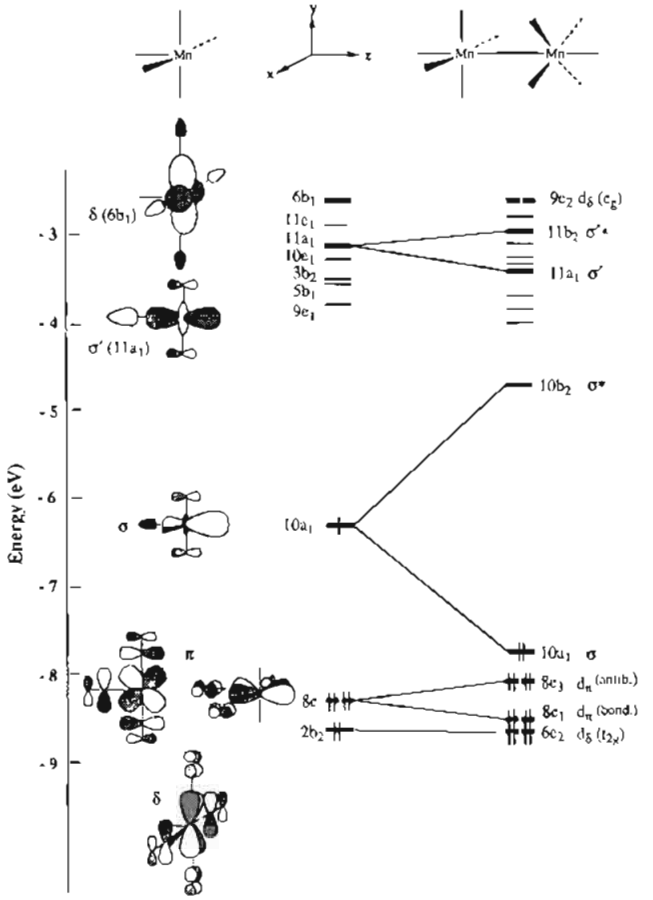

Figure 3. Orbital interaction diagram for dimerization of $Mn(CO)_5$.

These investigations mainly deal with the nature of the metal-metal bond in this prototype binuclear complex. However, as the nature of the excited states, which accounts for the photochemistry of $Mn_2(CO)_{10}$, depends on the character of the MOs involved in the excitations, we will give here a comprehensive description of the ground state MO composition. To this purpose it is instructive to look first at the frontier orbitals of the C_{4v} $Mn(CO)_5$ fragments from which $Mn_2(CO)_{10}$ is built up. On the left of the interaction diagram of Figure 3, where the metal centered d block of orbitals is reported for the $Mn(CO)_5$ fragment, we find a lower group of three "t_{2g}" like orbitals, labeled as $2b_2$ (d_{xy}) and 8e (d_{xz}, d_{yz}) in the C_{4v} point group of the fragment. Both $2b_2$ and 8e are involved in back-donation interactions with the ligands and, as schematically shown in Figure 3, are in-phase combinations between metal d_π and $2\pi^*$ orbitals of the CO ligands. However, while the d_{xy} ($2b_2$) provides backbonding to all four equatorial carbonyls, the d_{xz}, d_{yz} of the 8e set only interacts with the axial and two of the four equatorial carbonyl ligands. The consequence is that $2b_2$ lies ~0.5 eV below the 8e set.

Above the "t_{2g}" like orbitals, we do not just find two d orbitals descedent from the "e_g" set,[47] but three orbitals with $3d(e_g)$ character, i.e. the occupied $10a_1$ $3d_{z^2}$, $4p_z$ hybrid and higher in energy the unoccupied $11a_1$ with considerable $3d_{z^2}$ character and the $6b_1$ $3d_{x^2-y^2}$ ($d\delta(e_g)$). The remaining orbitals

(36) MacNeil, J. H.; Chiverton, A. C.; Fortier, S.; Baird, M. C.; Hynes, R. C.; Williams, A. J.; Preston, K. F.; Ziegler, T. *J. Am. Chem. Soc.* **1991**, *113*, 9834.
(37) Almenningen, A.; Jacobsen, G. G.; Seip, H. M. *Acta Chem. Scand.* **1969**, *23*, 685.
(38) Dahl, L. F.; Rundle, R. E. *Acta Crystallogr.* **1963**, *16*, 419.
(39) Martin, M.; Rees, B.; Mitschler, A. *Acta Crystallogr.* **1982**, *B38*, 6.
(40) Folga, E.; Ziegler, T. *J. Am. Chem. Soc.* **1993**, *115*, 5169.
(41) Fan, L.; Ziegler, T. *J. Chem. Phys.* **1991**, *95*, 7401.
(42) Fan, L.; Ziegler, T. *J. Chem. Phys.* **1992**, *96*, 9005.
(43) Fan, L.; Ziegler, T. *J. Phys. Chem.* **1992**, *96*, 6937.
(44) Fan, L.; Ziegler, T. *J. Am. Chem. Soc.* **1992**, *114*, 10890.
(45) Veillard, A.; Rhomer, M.-M. *Int. J. Quantum Chem.* **1992**, *42*, 965.
(46) Brown, D. A.; Chambers, W. J.; Fitzpatrick, N. J.; Rawlinson, R. M. *J. Chem. Soc. A* **1971**, 720.
(47) Elian, M.; Hoffmann, R. *Inorg. Chem.* **1975**, *14*, 1058.
(48) Heijser, W.; Baerends, E. J.; Ros, P. *Discuss. Faraday Soc. (Symp.)* **1980**, *14*, 211.
(49) Nakatsuji, H.; Hada, M.; Kawashima, A. *Inorg. Chem.* **1992**, *31*, 1740.
(50) Márquez, A.; Sanz, J. F.; Gelizé, M.; Dargelos, A. *J. Organomet. Chem.* **1992**, *434*, 235.

Table 1. One-Electron Energies and Percent Composition (Based on Mulliken Population Analysis per MO) of the Lowest Unoccupied and Highest Occupied $Mn_2(CO)_{10}$ Orbitals in Terms of Mn, CO_{ax}, and CO_{eq} Fragments. The Mn−Mn, Mn−CO_{ax}, and Mn−CO_{eq} Mulliken Overlap Populations Are Also Given.

orbital	ϵ (eV)	Mn	CO_{ax}	CO_{eq}	P^a(Mn−Mn)	P^a(Mn−CO_{ax})	P^a(Mn−CO_{eq})
			Unoccupied Orbitals				
$2a_2$	−2.29			100.0 (2π)			
$2b_1$	−2.47			100.0 (2π)			
$11e_3$	−2.48	5.3 d_π	14.4 (2π)	80.3 (2π)	−0.004	0.072	−0.074
$9e_2$	−2.98	49.7 $d\delta(e_g)$		50.3 (5σ)	−0.006		−0.246
$11e_1$	−3.00	1.5	68.0 (2π)	30.5 (2π)	0.028	0.070	−0.058
$11b_2$	−3.03	30.8(d_{z^2})	16.3 (5σ)	52.9 (2π)	−0.009	−0.100	−0.028
$10e_3$	−3.11	21.4 d_π	69.1 (2π)	9.5 (2π)	−0.046	−0.084	−0.030
$8e_2$	−3.36	14.0 $d\delta(t_{2g})$		86.0 (2π)	0.004		−0.068
$10e_1$	−3.37	30.0 d_π	15.7 (2π)	54.3 (2π)	0.056	−0.044	−0.108
$11a_1$	−3.41	30.8 (d_{z^2})	16.9 (5σ)	52.3 (2π)	0.144	−0.202	−0.018
$9e_1$	−3.81	4.2	1.5	96.1 (2π)	0.008	0.014	−0.018
$7e_2$	−3.87	21.6 $d\delta(t_{2g})$		78.4 (2π)	0.006		0.094
$9e_3$	−4.02	3.3	1.0	95.7 (2π)	−0.088	0.004	−0.024
$10b_2$	−4.79	47.5 (34.8 d_{z^2}, 12.7 p_z)	2.5	50.0 (2π)	−0.630	−0.004	0.015
			Occupied Orbitals				
$10a_1$	−7.87	57.0 (32.7 d_{z^2}, 24.3 p_z)	3.0	40.0 (2π)	0.145	0.004	0.034
$8e_3$	−8.06	72.0 d_π	13.0 (2π)	15.0 (2π)	−0.084	0.034	0.008
$8e_1$	−8.52	67.7 d_π	12.1 (2π)	20.2 (2π)	0.068	0.016	0.026
$6e_2$	−8.52	64.3 $d\delta(t_{2g})$		35.7 (2π)	−0.002		0.032

[a] The overlap populations are per bond. For the empty orbitals they have been calculated as though there were two electrons. [b] The nature of contributions of more than 10% is reported in parentheses.

in the virtual spectrum are either virtually 100% CO $2\pi^*$, such as 9e, $5b_1$, 11e, and $2a_2$, or have ca. 30% metal d character ($3b_2$ and 10e); i.e. they are just the 3d-2π π-antibonding partners of the occupied $2b_2$ and 8e. The latter orbitals are not of special interest to us, but since the $10a_1$, $11a_1$, and $6b_1$ orbitals play an important role in the photochemistry, it is useful to elucidate their composition. There are several remarkable features that can be observed in Table 1, which gives the composition of the plus and minus combinations that these orbitals form in $Mn_2(CO)_{10}$, the $10a_1(Mn(CO)_5)$ leading to $10a_1$ and $10b_2$, the $11a_1$ to $11a_1$ and $11b_2$ and the $6b_1$ to $9e_2$. These orbitals are plotted in Figures 4−6. The $6b_1$ is just the $d\delta(e_g)$, lying at high energy due to the strong antibonding with the equatorial CO 5σ's, which also causes a large negative Mn−CO_{eq} overlap population (see Table 1). This orbital needs no further comment, but let us note the following remarkable features for the a_1 orbitals: there are *two* a_1 orbitals with considerable $3d_{z^2}$ character; $10a_1$ has much $4p_z$ character, $11a_1$ virtually none; $10a_1$ has very little $5\sigma_{ax}$ character and is not Mn−CO_{ax} antibonding (virtually nonbonding), whereas $11a_1$ has considerable 5σ character and is strongly Mn−CO_{ax} antibonding; both $10a_1$ and $11a_1$ have much $2\pi_{eq}$ character (the largest contribution in terms of the Mulliken gross population), however with opposite phase (with respect to d_{z^2}) in $10a_1$ and $11a_1$ respectively (see Figures 4 and 5). These observations bring us to realize that the salient point in understanding the orbital structure is that, apart from $3d_{z^2}$, $4p_z$ and the a_1 combination of $2\pi_{eq}$ also play a key role. This is caused by the fact that the $4p_z$ overlaps strongly with the a_1 combination of $2\pi_{eq}$ ($S = 0.66$) resulting in a low-lying bonding combination of these orbitals.

Scheme 1 depicts the qualitative orbital interaction that we may invoke to explain the observations above. We start with $3d_{z^2}$ and $4p_z$ AOs that have been destabilized by antibonding with the CO_{ax} 5σ, the contribution of $5\sigma_{ax}$ to $3d_{z^2}$ (distinguished by the d subscript) being larger than the $5\sigma_p$ contribution of 5σ to $4p_z$. These orbitals straddle the $2\pi_{eq}$. In step 1 we allow the only strong orbital interaction to take place, i.e. the $2\pi_{eq}$ with $4p_z$ mixing. This will bring the bonding combination $2\pi_{eq}$ + $4p_z$ ($+5\sigma_p$), which is essentially a $2\pi_{eq}$ pushed down by $4p_z$, close to the $3d_{z^2}$ ($-5\sigma_d$). We cannot unequivocally determine the order of these two levels in this intermediate step from the final orbital composition, but it is clear that they must be pictured so close that considerable mixing will occur in step 2. The stabilized orbital that results from this mixing is the well-known

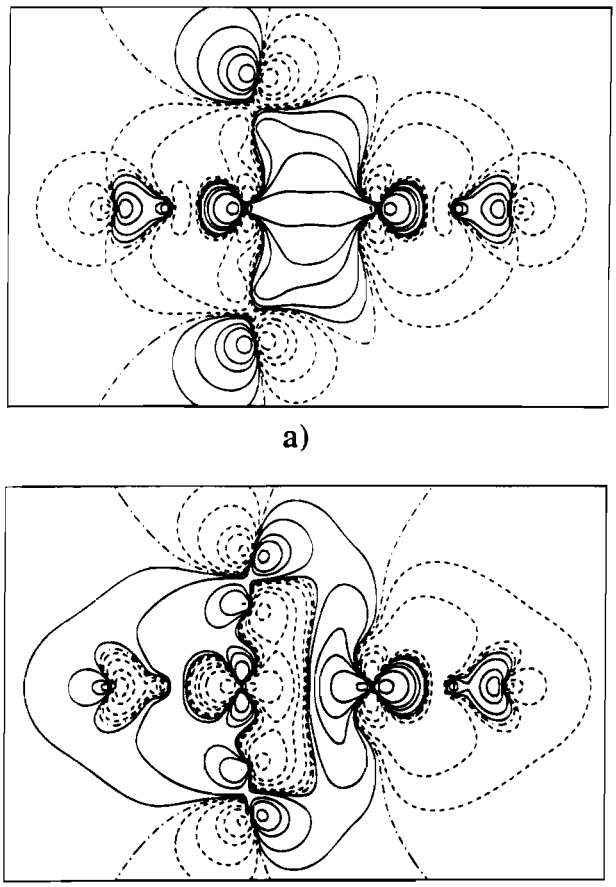

Figure 4. Contour plots of (a) $Mn_2(CO)_{10}$ $10a_1$ Mn−Mn σ-bonding and (b) $10b_2$ Mn−Mn σ-antibonding orbitals in a diagonal plane, containing the Mn atoms, two equatorial and the axial carbonyl groups (the orientation of the molecule is as in Figure 1). Contour values are 0.0, ±0.02, ±0.05, ±0.1, ±0.2, and ±0.5 [e/bohr^3]$^{1/2}$.

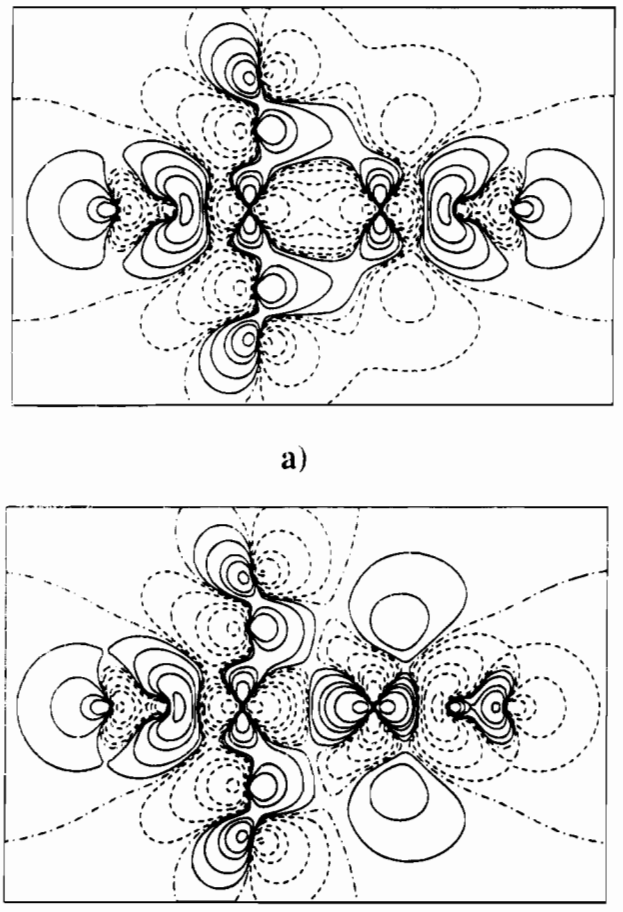

Figure 5. Contour plots of (a) $Mn_2(CO)_{10}$ $11a_1$ Mn−Mn σ'-bonding and (b) $11b_2$ Mn−Mn σ'-antibonding orbitals in a diagonal plane, containing the Mn atoms, two equatorial and the axial carbonyl groups. Contours: see caption to Figure 4.

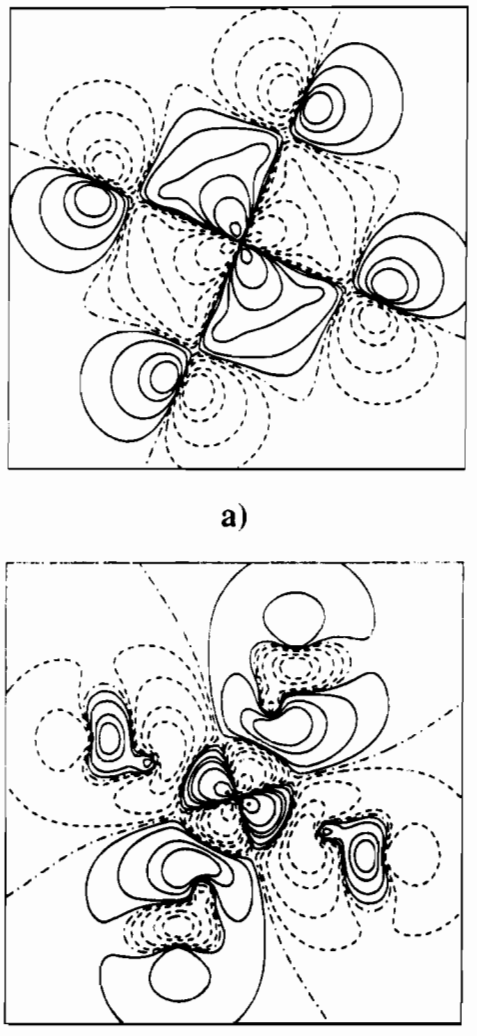

Figure 6. Contour plots of (a) $Mn_2(CO)_{10}$ $6e_2$ Mn−CO_{eq} π-bonding orbital and (b) $9e_2$ Mn−CO_{eq} σ-antibonding orbital in the xy plane at $z = 2.71$ au. Contours: see caption to Figure 4.

"hybrid" $10a_1 = 2\pi_{eq} + 3d_{z^2} + 4p_z$ $(-5\sigma_d + 5\sigma_p)$ (we list the AOs in order of importance, with small contributions in parentheses). The large $2\pi_{eq}$ and $4p_z$ contributions to this orbital, which contains the unpaired electron in $Mn(CO)_5$, was already evident from the contour plot in ref 48. Note the partial cancellation of 5σ contributions, leading to a small total $5\sigma_{ax}$ contribution, antibonding with $3d_{z^2}$ but bonding with $4p_z$, and hence a very small Mn−CO_{ax} overlap population in $10a_1$ (cf. $10a_1$ in Table 1).

The Mulliken populations in Table 1 are one way to analyse the orbitals. These populations are in substantial agreement with the composition expressed in terms of expansion coefficients, but may give a somewhat different emphasis. For instance, the largest coefficients of the fragment orbitals in $10a_1$ (of $Mn_2(CO)_{10}$) are as follows: +0.2326 $(4p_z - 4p_z)$; +0.3910 $(d_{z^2} + d_{z^2})$; −0.0997 $(5\sigma_{ax}{}^{left} + 5\sigma_{ax}{}^{right})$; +0.1510 $[(2\pi_1 + 2\pi_2 + 2\pi_3 + 2\pi_4)^{left} + (2\pi_1 + 2\pi_2 + 2\pi_3 + 2\pi_4)^{right}]$. In $10b_2$ they are as follows: +0.3359 $(4p_z + 4p_z)$; + 0.4716 $(d_{z^2} - d_{z^2})$; −0.0424 $(5\sigma_{ax}{}^{left} - 5\sigma_{ax}{}^{right})$; +0.2295 $[(2\pi_1 + 2\pi_2 + 2\pi_3 + 2\pi_4)^{left} - (2\pi_1 + 2\pi_2 + 2\pi_3 + 2\pi_4)^{right}]$. Here $2\pi_i$ denotes the 2π orbital on the ith equatorial CO, in the Mn−Mn−CO_i plane, with a positive lobe at C pointing toward the opposite Mn. The CO_{ax}−5σ contribution in these orbitals, which almost disappears in the Mulliken gross population, is still seen in the plots of Figure 4, in agreement with its nonnegligible coefficient.

The $11a_1$ of $Mn(CO)_5$ results from two effects, destabilizing antibonding mixing of the $3d_{z^2}$ $(-5\sigma_d)$ and the $2\pi_{eq} + 4p_z$ $(+5\sigma_p)$ (determined by the $2\pi_{eq} + 4p_z$ with $5\sigma_d$ and the $3d_{z^2}$ with $5\sigma_p$ interactions) and pushing down by the $4p_z - 2\pi_{eq}$ $(+5\sigma_p)$. Note that the 4p contributions cancel each other but the $2\pi_{eq}$ contributions reinforce each other, resulting in the large $2\pi_{eq}$ contribution observed in $11a_1$ (cf. $11a_1$ and $11b_2$ in Table 1 and Figure 5). Note that in this orbital the $2\pi_{eq}$ has a phase with respect to the d_{z^2} that is opposite to the one in $10a_1$. Note also that considerable $5\sigma_{ax}$ character remains, its antibonding with $3d_{z^2}$ not being diminished by bonding with $4p_z$, hence giving the large negative Mn−CO_{ax} overlap population in $11a_1$ and $11b_2$. The reversal of phase of the $2\pi_{eq}$ mentioned earlier implies that the $5\sigma_{ax}$ will also be antibonding with the equatorial COs. The large amount of $5\sigma_{ax}$ and its antibonding with both d_{z^2} and $2\pi_{eq}$ are clearly visible in the orbital plots of Figure 5. The largest coefficients of the fragment orbitals in $11a_1$ (of $Mn_2(CO)_{10}$) are as follows: +0.4478 $(d_{z^2} + d_{z^2})$; −0.5084 $(5\sigma_{ax}{}^{left} + 5\sigma_{ax}{}^{right})$; −0.2632 $[(2\pi_1 + 2\pi + 2\pi_3 + 2\pi_4)^{left} + (2\pi_1 + 2\pi + 2\pi_3 + 2\pi_4)^{right}]$. In $11b_2$ they are as follows: +0.4941 $(d_{z^2} - d_{z^2})$; −0.5031 $(5\sigma_{ax}{}^{left} - 5\sigma_{ax}{}^{right})$; −0.256550 $[(2\pi_1 + 2\pi_2 + 2\pi_3 + 2\pi_4)^{left} - (2\pi_1 + 2\pi_2 + 2\pi_3 + 2\pi_4)^{right}]$.

The interactions that follow upon building up $Mn_2(CO)_{10}$ from two $Mn(CO)_5$ units are displayed schematically in Figure 3 and some quantitative information is given in Table 1. This shows a population analysis of *all* the 3d and 2π derived orbitals in terms of Mn, CO_{eq}, and CO_{ax} fragment orbitals. The seven

Scheme 1

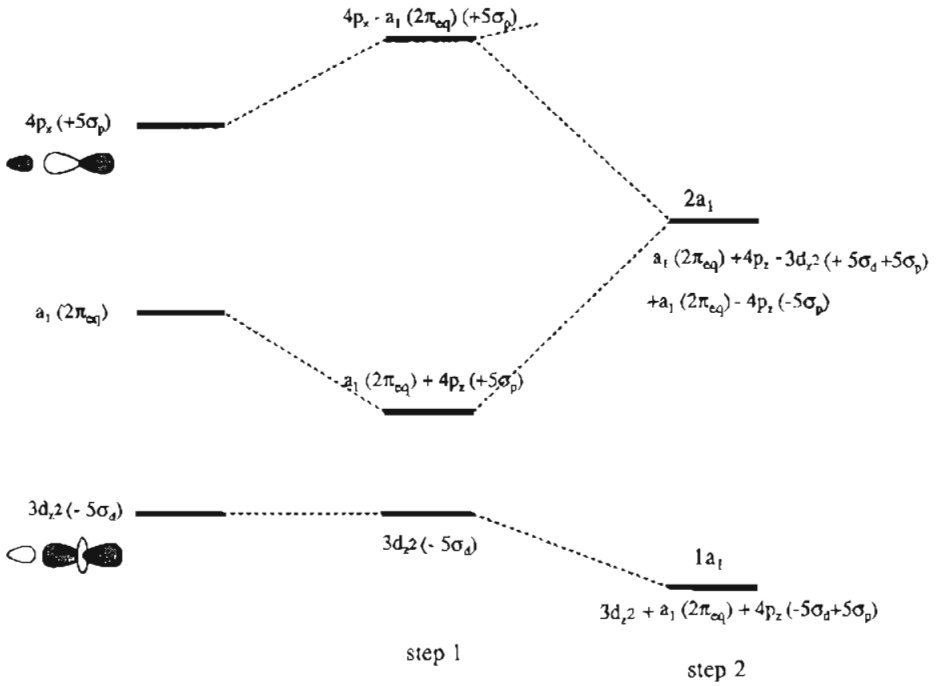

highest occupied orbitals of $Mn_2(CO)_{10}$, labeled as $6e_2$, $8e_1$, $8e_3$, and $10a_1$, lie well above (~3 eV) the other occupied orbitals and have about 60% Mn character. The $6e_2$, $8e_1$, and $8e_3$ are "t_{2g}" orbitals that are strongly 3d(Mn)−2π(CO) bonding. The d orbitals neatly partition into σ (d_{z^2}), π (d_{xz}, d_{yz}), and δ (d_{xy}, $d_{x^2-y^2}$) symmetries with respect to the Mn−Mn (z−) axis. It should be noted that, owing to the staggered conformation of the dimer, the pairwise splitting of σ and π $Mn(CO)_5$ orbitals into $Mn_2(CO)_{10}$ σ,σ* (a_1, b_2) and π, π* (e_1, e_3) does not occur for the δ type orbitals. The low-lying dδ(t_{2g}) orbitals d_{xy}^{left} and $d_{x^2-y^2}^{right}$ (i.e. two b_2 orbitals in the local C_{4v} symmetries of the $Mn(CO)_5$ monomers) have an overlap of zero due to the rotation over 45° of the $Mn(CO)_5$. These two orbitals form + and − combinations that do not split in energy but constitute the two components of an e_2 set in the D_{4d} symmetry of $Mn_2(CO)_{10}$. This is the low-lying $6e_2$, strongly Mn−CO_{eq} π bonding; see Figure 6a. The four $d_\pi(t_{2g})$ orbitals of the $Mn(CO)_5$ monomers form an e_1 set that is Mn−Mn π bonding and an e_3 combination that is π antibonding. The splitting between the resulting $8e_1$ and $8e_3$ is only ca. 0.5 eV due to the small d−d overlap. This stabilizes the bonding d_π (t_{2g}) combination $8e_1$ just enough to make it degenerate with the dδ (e_g) type $6e_2$ (see Table 1). It is interesting to observe that this pattern of one-electron energies mimicks quite nicely the pattern of ionization energies,[51] the ionizations out of $8e_1$ and $6e_2$ being degenerate (9.03 eV) and the $8e_1$ ionization energy being ca. 0.7 eV lower (8.35 eV).

The orbitals that come next are the HOMO $10a_1$ (experimental[51] ionization energy 8.02 eV), accounting for the formally single metal−metal bond, and the LUMO $10b_2$. The Mn−Mn σ-bond is not so much a d_{z^2}−d_{z^2} bond, but more a $4p_z$−$4p_z$ and $2\pi_{eq}$−$2\pi_{eq}$ bond (cf. Figure 4a). Since the d−d overlaps are small (ca. 0.03 for both d_{z^2}−d_{z^2} and d_π−d_π) and the $4p_z$−$4p_z$ overlap (0.405) and $2\pi_{eq}$−$2\pi_{eq}$ overlap (0.229 between normalized A_u combinations) much larger, the σ, σ* splitting between $10a_1$ and $10b_2$ is large compared to the π, π* one (3 eV *vs* 0.5 eV). Note also that the Mn−Mn bond does not fall in the normal range (2.40−2.70 Å) of metal−metal single bonds, but is rather long (about 2.9 Å), in keeping with the diffuse nature of the primary bonding orbitals $4p_z$ and $2\pi_{eq}$. Owing to the peculiar nature of the $Mn(CO)_5$ $10a_1$ "hybrid", the $Mn_2(CO)_{10}$ $10a_1$ HOMO orbital shows a high amplitude between the two $Mn(CO)_5$ monomers, while its antibonding counterpart, the $10b_2$ LUMO is conspicuously antibonding between these fragments (see plots of Figure 4).

Besides the Mn−Mn bond length, another (related) point of interest concerning the structure of $Mn_2(CO)_{10}$ is the bending of the four equatorial carbonyls on each Mn atom toward the other Mn atom (with a C_a−Mn−C_{eq} angle of 94° in the structure by Martin *et al.*[39]). This fact has been considered as an indication that the equatorial carbonyls have some bridging function. This question is still controversial.[45] Of course the bending of the equatorial carbonyls observed in $Mn_2(CO)_{10}$ does not necessarily originate from cross-interactions between the metal and the carbonyls not directly bonded to it, since the bending is already present in $Mn(CO)_5$. On the other hand, the $Mn(CO)_5$ $10a_1$ has considerable $4p_z$ and $2\pi_{eq}$ character and there will be considerable overlap between these orbitals on the two monomers, which implies the presence of Mn−CO_{eq} cross interactions as well as CO_{eq}−CO_{eq} interactions in the $10a_1$ (e.g. the $a_1(2\pi_{eq})$−$a_1(2\pi_{eq})$ overlap is 0.23, the $4p_z$−$a_1(2\pi_{eq})$ overlap is 0.66). A full assessment would however also have to take into account the CO_{eq}−CO_{eq} steric repulsion.

The virtual spectrum from $9e_3$ upwards consists of the predominantly CO $2\pi^*$ orbitals and the only 3d orbitals left, the dδ(e_g) orbitals $d_{x^2-y^2}^{left}$, d_{xy}^{right}. Again, these dδ orbitals (more precisely two b_1 orbitals in the local C_{4v} symmetries of the $Mn(CO)_5$ monomers) have overlap zero due to the rotation over 45° of the $Mn(CO)_5$. They form + and − combinations that do not split in energy but constitute the two components of an e_2 set in the D_{4d} symmetry of $Mn_2(CO)_{10}$. This is the high-lying $9e_2$, strongly antibonding with the 5σ's of the equatorial COs (see Figure 6b). The virtual CO $2\pi^*$ spectrum extends over a range of about 1.7 eV. Some of the e_2, e_1, and e_3 orbitals have considerable Mn 3d admixture, in accordance with their interpretation as antibonding counterparts to the Mn−CO π bonding $6e_2$−$8e_3$. A remarkable feature is the high d_{z^2}

(51) Evans, S.; Green, J. C.; Green, M. L. H.; Orchard, A. F.; Turner, D. W. *Discuss. Faraday Soc.* **1969**, *54*, 112.

Table 2. Electronic Transitions (in cm^{-1}) for $Mn_2(CO)_{10}$ with Experimental Absorption Bands from Ref 25

type	transitions	state	energy	experimental bands
$\sigma \rightarrow \sigma^*$	$10a_1 \rightarrow 10b_2$	a^3B_2	23 039	
$d_\pi \rightarrow \sigma^*$	$8e_3 \rightarrow 10b_2$	a^3E_1	27 134	
$\sigma \rightarrow \sigma^*$	$10a_1 \rightarrow 10b_2$	a^1B_2	27 336[a]	26 700 (band I)
$d_\pi \rightarrow \sigma^*$	$8e_3 \rightarrow 10b_2$	a^1E_1	28 982[a]	29 740 (band II)
$\sigma \rightarrow \pi^*$	$10a_1 \rightarrow 9e_1$	b^3E_1	32 398	
$\sigma \rightarrow \pi^*$	$10a_1 \rightarrow 9e_1$	b^1E_1	32 945[a]	
$d_\pi \rightarrow \pi^*$	$8e_3 \rightarrow 7e_2$	c^3E_1	35 031	
$d_\pi \rightarrow \pi^*$	$8e_3 \rightarrow 9e_1$	b^3B_2	36 061	
$d_\pi \rightarrow \pi^*$	$8e_3 \rightarrow 7e_2$	c^1E_1	36 197[a]	
$d_\pi \rightarrow \pi^*$	$8e_3 \rightarrow 9e_1$	b^1B_2	36 515[a]	
$\sigma \rightarrow \pi^*$	$10a_1 \rightarrow 10e_1$	d^3E_1	36 603	
$\sigma \rightarrow \pi^*$	$10a_1 \rightarrow 10e_1$	d^1E_1	37 099[a]	
$d_\pi \rightarrow \pi^*$	$8e_3 \rightarrow 10e_1$	c^3B_2	38 160	
$d_\pi \rightarrow \pi^*$	$8e_1 \rightarrow 7e_2$	e^3E_1	38 395	
$\sigma \rightarrow \pi^*$	$10a_1 \rightarrow 11e_1$	f^3E_1	38 613	
$d_\pi \rightarrow \pi^*$	$6e_2 \rightarrow 9e_3$	g^3E_1	38 633	
$d_\pi \rightarrow \pi^*$	$8e_1 \rightarrow 9e_3$	d^3B_2	42 168	
$\sigma \rightarrow \sigma'^*$	$10a_1 \rightarrow 11b_2$	e^3B_2	38 900	
$d_\pi \rightarrow \pi^*$	$6e_2 \rightarrow 9e_3$	e^1E_1	39 279[a]	37 600 (band III)
$d_\pi \rightarrow \pi^*$	$8e_1 \rightarrow 7e_2$	f^1E_1	39 460[a]	
$d_\pi \rightarrow \pi^*$	$6e_2 \rightarrow 9e_1$	h^3E_1	40 347	
$d_\pi \rightarrow \pi^*$	$6e_2 \rightarrow 9e_1$	g^1E_1	40 949[a]	
$d_\pi \rightarrow \pi^*$	$8e_3 \rightarrow 10e_1$	c^1B_2	41 317[a]	
$\sigma \rightarrow \pi^*$	$10a_1 \rightarrow 11e_1$	h^1E_1	41 645[a]	
$d_\pi \rightarrow \pi^*$	$6e_2 \rightarrow 7e_2$	f^3B_2	41 945	
$\sigma \rightarrow \sigma'^*$	$10a_1 \rightarrow 11b_2$	d^1B_2	41 955	
$d_\pi \rightarrow \pi^*$	$8e_1 \rightarrow 9e_3$	e^1B_2	42 754[a]	
$d_\pi \rightarrow \sigma^*$	$8e_3 \rightarrow 11b_2$	i^3E_1	43 066	
$d_\pi \rightarrow \sigma^*$	$8e_1 \rightarrow 11a_1$	j^3E_1	44 105	
$d_\pi \rightarrow \sigma^*$	$8e_3 \rightarrow 11b_2$	i^1E_1	44 148[a]	
$d_\pi \rightarrow \sigma^*$	$8e_1 \rightarrow 11a_1$	j^1E_1	45 190[a]	
$d_\pi \rightarrow \pi^*$	$8e_1 \rightarrow 10e_3$	g^3B_2	45 626	
$d_\pi \rightarrow \pi^*$	$6e_2 \rightarrow 7e_2$	f^1B_2	46 095[a]	
$d_\pi \rightarrow \pi^*$	$8e_1 \rightarrow 8e_2$	k^3E_1	47 575	
$d_\pi \rightarrow d\delta(e_g)$	$6e_2 \rightarrow 9e_2$	h^3B_2	47 636	
$d_\pi \rightarrow \pi^*$	$6e_2 \rightarrow 8e_2$	i^3B_2	47 640	
$d_\pi \rightarrow \pi^*$	$8e_1 \rightarrow 8e_2$	k^1E_1	47 940[a]	
$d_\pi \rightarrow \pi^*$	$8e_1 \rightarrow 10e_3$	g^1B_2	48 205[a]	
$d_\pi \rightarrow \pi^*$	$6e_2 \rightarrow 8e_2$	h^1B_2	49 383[a]	
$d_\pi \rightarrow d\delta(e_g)$	$6e_2 \rightarrow 9e_2$	i^1B_2	49 517[a]	

[a] Symmetry allowed.

content of the $11a_1$ and $11b_2$ orbitals, which can be fully explained from the composition of the parent $Mn(CO)_5-11a_1$ orbitals discussed above. They are Mn−Mn bonding, resp. antibonding, σ orbitals (see plots of Figure 5). Since the Mn part of these orbitals is purely d_{z^2} and lacks the $4p_z$ component the energy splitting of 0.4 eV is comparable to a splitting induced by 3d−3d interaction such as $8e_1-8e_3$, and not like the $10a_1-10b_2$ σ,σ^* splitting. We have noted before that these orbitals, hereafter denoted as σ' and σ'^*, are quite strongly antibonding with respect to the axial carbonyl ligands (cf. plots of Figure 5 and overlap populations in Table 1). We will discuss below the importance of the $Mn-CO_{ax}$ σ-antibonding nature of $11a_1$ and $11b_2$ for the photochemistry of $Mn_2(CO)_{10}$.

$Mn_2(CO)_{10}$ Excited States

Since the occupied 3d orbitals lie ~3 eV above the other orbitals, only the d set ($6e_2$, $8e_1$, $8e_3$, $10a_1$) needs to be considered as the origin of the excitations at relatively low energy, which are of interest for the photochemistry of this complex. Two transitions are fully allowed in the D_{4d} symmetry of $Mn_2(CO)_{10}$, $^1A_1 \rightarrow {}^1B_2$ and $^1A_1 \rightarrow {}^1E_1$. However, the excitations leading to triplet $^3B_2$ and $^3E_1$ excited states should be also considered, given the important role that triplet states may play in the photochemistry. The calculated excitation energies to the triplet and singlet excited states of symmetry B_2 and E_1, up to 50 000 cm^{-1}, are reported in Table 2 together with the experimental absorption bands. We find that the lowest excited state at 23 039 cm^{-1} is a triplet $^3B_2$ corresponding to the $\sigma \rightarrow \sigma^*$ transition. Its singlet component is found about 4300 cm^{-1} higher. Next, respectively at 28 982 and 27 134 cm^{-1} we find the singlet $^1E_1$ and the triplet $^3E_1$ components of the $8e_3 \rightarrow 10b_2$ transition, that, owing to the large CO contribution to the $10b_2$ orbital (about 50%), may be classified as MLCT rather than as a ligand field transition. A number of triplet and singlet states corresponding to MLCT transitions, mostly of $d_\pi \rightarrow \pi^*$ type, (the triplet state being usually at about 500−2000 cm^{-1} below the corresponding singlet state) fall above 30 000 cm^{-1}.

Unfortunately, direct comparison of calculated with experimental transitions is somewhat difficult, since the experimental spectrum of $Mn_2(CO)_{10}$ in solution is poorly resolved.[25] It is characterized by a four band system: a broad and relatively intense band (band II) centered at around 29 740 cm^{-1}, a shoulder to the red of this band at 26 700 cm^{-1} which is not resolved at room temperature (band I), a weak and broad band spanning the region between 35 000 and 40 000 cm^{-1} (band III), then an intense and featureless band at ≈50 000 cm^{-1} (band IV). Gray *et al.*[25] have assigned band II to the $^1A_1 \rightarrow {}^1B_2$ ($\sigma \rightarrow \sigma^*$) dipole-allowed transition, on the basis of a combination of energetic and polarization arguments. The same arguments are used by these authors to assign the weak shoulder to the red of the band to the $^1A_1 \rightarrow {}^1E_1$ ($d_\pi \rightarrow \sigma^*$) transition. A number of MLCT transitions are believed to be responsible for the absorption corresponding to band III.

The computed energy of the singlet state $^1E_1$ corresponding to the $8e_3 \rightarrow 10b_2$ ($d_\pi \rightarrow \sigma^*$) transition agrees with the experimental band II maximum. In turn the energy of the singlet $^1B_2$ corresponding to the $\sigma \rightarrow \sigma^*$ transition matches quite well with the experimental band I. That the $^1B_2$ excited state is lower than the $^1E_1$ in our calculation indicates that, although electronic relaxation effects are more effective for the $d_\pi \rightarrow \sigma^*$ ($8e_3 \rightarrow 10b_2$) transition, nevertheless they are not large enough to overcome the energy difference between the $10a_1$ and $8e_3$ one-electron levels that both photoelectron spectroscopy and theoretical calculations,[25,46-51] including the present one, give in the order $10a_1 > 8e_3$. On the basis of our calculations it seems reasonable to assign the lowest experimental band (band I) to the $^1A_1 \rightarrow {}^1B_2$ ($\sigma \rightarrow \sigma^*$) transition and the more intense (band II) to the $^1A_1 \rightarrow {}^1E_1$ ($d_\pi \rightarrow \sigma^*$) transition. Our assignment contradicts the suggestion by Gray *et al.*[25] according to whom the fact that the $d_\pi \rightarrow \sigma^*$ ($8e_3 \rightarrow 10b_2$) transition is lower in energy than the $\sigma \rightarrow \sigma^*$, in spite of the one-electron level ordering, is due to a smaller electronic rearrangement of the B_2 state compared to the E_1 state. The considerable MLCT character of this transition that we pointed out above provides some support for our assignment. Although the assumptions by Gray *et al.* are open to some criticism, as recently suggested by Márquez *et al.*,[50] a definitive assignment would require further investigations, both experimental (band polarizations) and theoretical (transition intensities).

However, apart from the controversial assignment of these bands, a significant point to arise from our calculations is that only two transitions, i.e. $d_\pi \rightarrow \sigma^*$ ($8e_3 \rightarrow 10b_2$) and $\sigma \rightarrow \sigma^*$ ($10a_1 \rightarrow 10b_2$) are responsible for bands I and II. The other transitions fall indeed well above 30 000 cm^{-1}. Excitation at low energy, in the experimental range of 337−355 nm will bring the molecule either into the $\sigma \rightarrow \sigma^*$ $^1B_2$ or into the ($8e_3 \rightarrow 10b_2$) $^1E_1$ spin allowed excited state. This would imply that the states arising from $d_\pi \rightarrow \sigma^*$ and $\sigma \rightarrow \sigma^*$ dominate the photochemistry of $Mn_2(CO)_{10}$ upon excitation in the range 337−355 nm. A number of states ascribed to band III will lead to

the photochemical reactivity of $Mn_2(CO)_{10}$ at higher energy. We will try to discuss the probability of the various types of photoreactivity using the orbital characters given above.

Focusing first on the nature of the states arising from $d_\pi \rightarrow \sigma^*$ ($8e_3 \rightarrow 10b_2$) and $\sigma \rightarrow \sigma^*$ ($10a_1 \rightarrow 10b_2$) transitions, we note that the Mn−Mn bonding and antibonding natures, respectively, of the σ and σ^* will doubtless make the state B_2 corresponding to the $\sigma \rightarrow \sigma^*$ transition photoactive with respect to metal−metal cleavage. It is unlikely that this state might also lead to axial CO loss, given the low contribution of the axial COs to these orbitals. Equatorial CO loss is also unlikely, given the $Mn-CO_{eq}$ π-bonding nature of both starting and arriving orbitals. The state E_1 corresponding to the $d_\pi-\sigma^*$ ($8e_3 \rightarrow 10b_2$) could in principle be responsible for $Mn-CO_{ax}$ as well as Mn−Mn cleavage, due to the loss of $Mn-CO_{ax}$ π-bonding character of the $8e_3$ and the activation of the Mn−Mn antibonding character of $10b_2$. However, two Mn−Mn bonding electrons remain in the σ orbital, so the bond is probably weakened but not broken. As far as axial CO loss is concerned, one wonders how effective the loss of one out of four $d_\pi-2\pi$ bonding electrons can be. Equatorial CO loss is unlikely for the same reason as above. However, even if the E_1 state corresponding to the $d_\pi \rightarrow \sigma^*$ ($8e_3 \rightarrow 10b_2$) excitation would not be photoactive by itself, neither for the dissociation of an axial ligand nor for the dissociation of an equatorial carbonyl ligand, photodissociation of a carbonyl ligand at low energy might still occur upon excitation to the $d_\pi \rightarrow \sigma^*$ ($8e_3 \rightarrow 10b_2$) E_1 state by crossing to the potential energy surfaces of excited states which *are* photoactive for the dissociation of a carbonyl ligand (see below). If such a crossing can occur and how large the barrier would be will have to follow from complete potential energy surface calculations. Intersection of the ($\sigma \rightarrow \sigma^*$) B_2 and ($8e_3 \rightarrow 10b_2$) E_1 surfaces may enable photoprocesses to occur independently of the excitation wavelength in the experimental range of 337−355 nm. The close proximity of the ($\sigma \rightarrow \sigma^*$) $^1B_2$ and ($8e_3 \rightarrow 10b_2$) $^{1,3}E_1$ states (with a calculated separation of 1646 and 203 cm^{-1} for the singlet and triplet respectively) would make intersystem crossing an easy process.

At higher energy, we can locate a number of states that may play a role in the photochemical reactivity of $Mn_2(CO)_{10}$. Most of these, however, should not have any dissociative character with respect to Mn−Mn cleavage, except perhaps for the B_2 corresponding to the $10a_1 \rightarrow 11b_2$ transition, although the very small negative overlap population indicates the Mn−Mn antibonding nature of $11b_2$ to be quite weak. Photochemical loss of an equatorial CO ligand may result in principle from $d\pi$, $d\delta \rightarrow \pi^*$, or $d\pi$, $d\delta \rightarrow d\delta(e_g)$ excitations which depopulate $Mn-CO_{eq}$ π-bonding orbitals and populate strongly $Mn-CO_{eq}$ π- or σ-antibonding orbitals. Given the strong σ-antibonding with equatorial CO in the $9e_2$ $d\delta(e_g)$, the $6e_2 \rightarrow 9e_2$, the $8e_1 \rightarrow 9e_2$, and the $8e_3 \rightarrow 9e_2$ satisfy this requirement. Equatorial CO loss on account of π antibonding in the virtual orbital might arise from several transitions, notably ones involving the $10e_1$, e.g. $10a_1 \rightarrow 10e_1$, $8e_3 \rightarrow 10e_1$, and $6e_2 \rightarrow 10e_1$. These excitations, except for the $6e_2 \rightarrow 9e_2$ and $8e_3 \rightarrow 10e_1$, lead to E_1 states.

Concerning the photochemical loss of an axial CO ligand in a high energy excitation, following the above suggestions, we may consider two transitons which depopulate $Mn-CO_{ax}$ π-bonding orbitals and populate $Mn-CO_{ax}$ σ-antibonding orbitals, i.e. $d_\pi \rightarrow \sigma'^*$ $8e_3 \rightarrow 11b_2$, and $d_\pi \rightarrow \sigma'$ $8e_1 \rightarrow 11a_1$. They involve the σ' and σ'^* orbitals shown in the plots of Figure 5 whose $Mn-CO_{ax}$ σ-antibonding nature has been already stressed. There are, furthermore, two $d_\pi \rightarrow \pi^*$ excitations which also might play a role in the photodissociation of the axial CO at high energy, $8e_3 \rightarrow 10e_1$ and $8e_1 \rightarrow 10e_3$.

Discussion

The present calculations of excitation energies of $Mn_2(CO)_{10}$ leave little doubt that only two excited states are responsible for the low-energy excitation (bands I and II) at 337−375 nm, ($\sigma \rightarrow \sigma^*$) B_2 and ($d\pi \rightarrow \sigma^*$) E_1. The order of these two states remains somewhat controversial, our calculated ordering contradicting the assignment by Levenson and Gray, but definitive assignment will require further investigation (notably intensity calculations). Although explicit calculation of PEC's for $Mn-CO_{ax}$ or $Mn-CO_{eq}$ bond elongation have to verify this, it seems unlikely that these states are dissociative with respect to Mn−CO. We have been able to identify LF type excitations to states that are probably $Mn-CO_{ax}$ dissociative (basically $d \rightarrow \sigma'$) and to states that are probably $Mn-CO_{eq}$ dissociative ($d \rightarrow d\delta(e_g)$). We confirm the Levenson−Gray assignment of the $d \rightarrow d\delta(e_g)$ excitation at much higher energy than the ($\sigma \rightarrow \sigma^*$) B_2, and we believe that assignment of the low-energy shoulder around 374 nm in the spectrum of $Mn_2(CO)_{10}$ to $d \rightarrow d$ excitation, a possibility discussed by Caspar and Meyer[24] can be ruled out. How, then, can the observation of CO dissociation upon low-energy excitation be explained? The only possibilities are that the ($\sigma \rightarrow \sigma^*$) B_2 or ($d\pi \rightarrow \sigma^*$) E_1 are Mn−CO dissociative, in contrast to our expectation, or the ($d \rightarrow \sigma'$) and/or ($d \rightarrow d\delta(e_g)$ excited states are so strongly dissociative that crossing can occur from a low energy excited state to the dissociative PEC of one of these high lying states. Explicit calculation of the PEC's will be carried out to distinguish between these possibilities.

IC940860E